

TreeDGS: Aerial Gaussian Splatting for Distant DBH Measurement

Belal Shaheen¹, Minh-Hieu Nguyen¹, Bach-Thuan Bui¹, Shubham¹, Tim Wu¹, Michael Fairley¹,
 Matthew David Zane¹, Michael Wu^{1*}, James Tompkin²
¹Coolant, ²Brown University

*Corresponding author: michael@coolant.earth

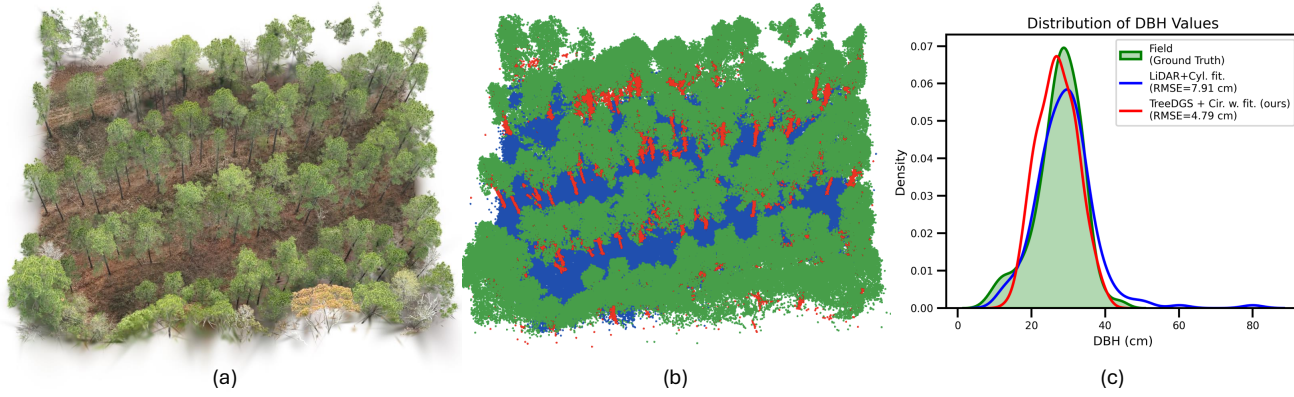


Figure 1. **TreeDGS: RGB-only for DBH estimation with 3D Gaussian Splatting.** (a) High-fidelity TreeDGS reconstruction from distant UAV RGB imagery as an optimized set of 3D Gaussians. (b) Surface points extracted via opacity-consistent sampling (built on RaDe-GS [50]) and segmented into stem vs. vegetation to isolate trunk geometry for DBH fitting. (c) DBH errors against field measurements, shown as the distribution of DBH estimates relative to the field DBH distribution; TreeDGS + opacity-weighted circle fitting reduces error vs. UAV LiDAR + cylinder fitting [32] (RMSE/MAE: 4.79/3.67 cm vs. 7.91/5.04 cm) at ground sample distance (GSD) of ≈ 1.84 cm.

Abstract

Aerial remote sensing enables efficient large-area surveying, but accurate direct object-level measurement remains difficult in complex natural scenes. Recent advancements in 3D vision, particularly learned radiance-field representations such as NeRF and 3D Gaussian Splatting, have begun to raise the ceiling on reconstruction fidelity and densifiable geometry from posed imagery. Nevertheless, direct aerial measurement of important natural attributes such as tree diameter at breast height (DBH) remains challenging. Trunks in aerial forest scans are distant and sparsely observed in image views: at typical operating altitudes, stems may span only a few pixels. With these constraints, conventional reconstruction methods leave breast-height trunk geometry weakly constrained. We present TreeDGS, an aerial image reconstruction method that leverages 3D Gaussian Splatting as a continuous, densifiable scene representation for trunk measurement. After SfM-MVS initialization and

Gaussian optimization, we extract a dense point set from the Gaussian field using RaDe-GS’s depth-aware cumulative-opacity integration and associate each sample with a multi-view opacity reliability score. Then, we estimate DBH from trunk-isolated points using opacity-weighted solid-circle fitting. Evaluated on 10 plots with field-measured DBH, TreeDGS reaches 4.79,cm RMSE (about 2.6 pixels at this GSD) and outperforms a state-of-the-art LiDAR baseline (7.91,cm RMSE). This shows that TreeDGS can enable accurate, low-cost aerial DBH measurement (Fig. 1).

1. Introduction

Aerial remote sensing has quickly become a cornerstone of modern environmental monitoring for its ability to survey large areas rapidly and cost efficiently [1, 7, 36]. Yet, despite major gains in sensor resolution, platform stability, and reconstruction pipelines, extracting direct, object-

level measurements from aerial imagery remains difficult in structurally complex natural scenes [8, 15]. Forested environments are challenging: heterogeneous geometry, self-similar textures, frequent occlusion, and strong appearance variability across lighting conditions all weaken the visual cues that aerial reconstruction methods rely upon [15].

A prominent example is tree diameter at breast height (DBH)—a foundational forestry variable that aerial remote sensing struggles to recover reliably. Its importance for forestry cannot be understated: DBH measures an individual tree’s size and growth stage, and is a primary input to standard allometric models and reporting workflows that estimate wood volume, biomass, and carbon [2, 5, 17, 18]. In turn, these allometric models underpin decision making used across forestry operations and policy, ranging from timber inventory and silvicultural planning to carbon offset quantification, wildfire risk mitigation, and long-term ecosystem management [3, 41].

DBH estimation from above-canopy aerial sensing is fundamentally constrained by observability. In typical UAV image surveys flown at operational altitudes, stems are not “large objects.” In our data, captured at ~ 70 m above ground (GSD ≈ 1.84 cm/px), stems in the evaluation plots span only ~ 15 pixels across per view on average (Tab. 1), and can be just a few pixels wide for smaller trees (Fig. 2). This pixel scarcity is compounded by view scarcity: the breast-height band ($h_{BH} \approx 1.37$ m in our field protocol) is frequently occluded by crowns, branches, and understory vegetation, so each stem may be seen only in a handful of oblique glimpses through noisy canopy gaps. Therefore, the core geometric challenge of measurement is recovering enough faithful breast-height trunk surface to support stable circle or cylinder fitting under a regime of few pixels, few views, and partial visibility.

Active sensing can mitigate some of these constraints by providing explicit range measurements rather than relying on image texture. Terrestrial laser scanning (TLS), for example, is well known to support robust DBH measurements because it can produce dense, well-populated stem cross-sections [20, 30, 38]. However, the mostly downward-looking trajectories of airborne or UAV laser scanning do not typically yield equally dense returns on the trunk at breast height: even with high point density, trunk hits near h_{BH} can be sparse, uneven, and contaminated by surrounding vegetation, complicating per-tree stem isolation and reliable fitting in cluttered stands [24, 25, 35]. These limitations help explain why aerial LiDAR has seen broader operational adoption for canopy structure and terrain products rather than for direct DBH measurement [6, 13, 31, 39, 47].

RGB-only UAV photogrammetry has nevertheless made substantial progress for other forest attributes, including canopy height models and structural mapping [8, 15, 44, 45]. But DBH remains difficult from aerial imagery alone,

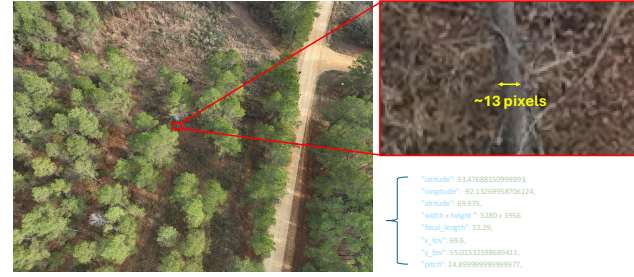


Figure 2. Pixel-limited trunk observations from distant aerial imagery. At ~ 70 m altitude (GSD ≈ 1.84 cm/px), a typical pine stem can occupy only ~ 13 pixels across in a single RGB image, making per-image diameter cues highly quantized, sensitive to occlusion, and difficult to measure precisely.

even under careful survey design with aggressive overlap and strong oblique views [34]. In the pixel- and view-limited regime described above, conventional SfM–MVS pipelines often fail to recover a coherent breast-height surface. Sparse SfM relies on repeatable keypoints and long feature tracks [40], but distant trunks provide weak texture and are frequently interrupted by foliage occlusions, yielding unstable or missing correspondences. View-dependent MVS densification [9] then tends to drop out on trunks when visibility is intermittent and texture cues are weak.

Recent radiance-field representations, such as Neural Radiance Fields (NeRF) [33] and 3D Gaussian Splatting (3DGS) [22], can improve reconstruction fidelity from posed imagery and offer a promising path forward for thin structures that are only weakly observed in individual frames. Early forestry applications have begun exploring radiance fields for forest monitoring and tree-scale reconstruction [14, 23, 27, 42], but the problem of direct DBH measurement from stand-off, above-canopy UAV surveys remains largely unaddressed. Moreover, translating a “fluffy” radiance-field reconstruction into a reliable diameter requires a measurement-oriented extraction step: a sufficiently dense sampling at breast height and a way to prioritize samples that are consistently supported across views. Most forestry applications of radiance fields to date have focused on close-range terrestrial [27] imagery which have a different set of constraints, leaving aerial DBH measurement largely unaddressed by radiance field methods.

We introduce TreeDGS: an aerial reconstruction pipeline that uses 3D Gaussian Splatting as a measurement-oriented scene representation for estimating DBH from commodity UAV RGB imagery under pixel- and view-limited trunk observations. Starting from standard SfM camera poses and an MVS initialization, we optimize a RaDe-GS model [50] to obtain a continuous Gaussian field whose covariances and opacities are refined by multi-view photometric consistency. Then, we extract a dense point set using depth-aware

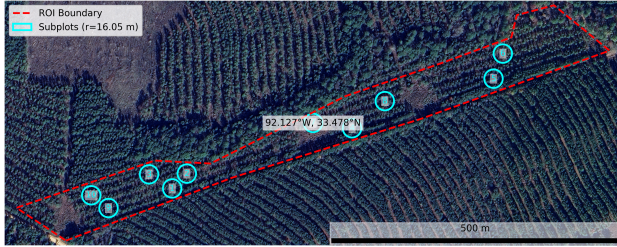


Figure 3. **Region of interest (ROI) and plot layout (10 subplots).** Each subplot corresponds to one 0.2-acre circular plot (radius 16.05 m). The circle indicates the field plot boundary used for tree inclusion, while the dashed polygon outlines the ROI used to clip and organize aerial products for per-plot processing.

cumulative-opacity integration, retaining samples whose accumulated opacity indicates a reliably occupied surface under a fixed threshold. To mitigate spurious samples from foliage and partial occlusions, we compute a per-point multi-view opacity support score as a reliability signal and retain trunk-isolated points via 3D semantic segmentation. Finally, we estimate DBH with opacity-weighted, slice-wise circle fitting, yielding diameter estimates even when the trunk is only weakly observed in individual images.

Our contributions are summarized as follows:

- We present TreeDGS, a method that directly reconstructs and measures DBH from above-canopy UAV RGB imagery by using a 3D Gaussian Splatting scene representation in a pixel-limited regime.
- We introduce a depth- and opacity-aware point extraction procedure based on RaDe-GS that densifies the Gaussian field into a surface-consistent point set and attaches a multi-view opacity support score, enabling reliability-weighted geometric fitting.
- We demonstrate real-world, field-validated performance in a managed loblolly pine forest with dense understory and varied growth patterns (10 plots), achieving 4.79 cm RMSE (~ 2.6 pixels at our GSD) against ground-truth tape DBH and outperforming an ultra-high-resolution UAV LiDAR baseline by 39.4% in RMSE.

2. Materials

Data were collected in a managed *Pinus taeda* (loblolly pine) stand in southeastern Arkansas, USA. We established ten 0.2-acre circular plots (plots 1–10; radius 16.05 m; Fig. 3). At each plot center, we marked a circular plot boundary with a 16.05 m radius and measured all stems within the boundary. Each included tree was assigned a unique ID. For each tree, we recorded: (i) bearing and distance from the plot center; (ii) DBH measured with a diameter tape at 1.37 m above ground level; and (iii) height measured using a laser rangefinder.

We surveyed plot centers using ORS/NTRIP network

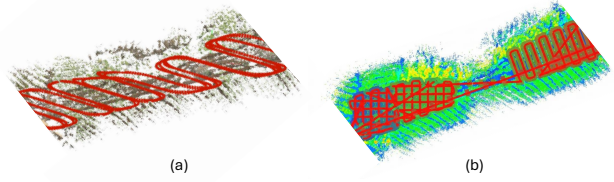


Figure 4. **RGB and LiDAR acquisition patterns.** (a) RGB imagery was collected with high overlap and mixed viewing angles to support SfM/MVS and improve trunk visibility. (b) LiDAR was flown with dense grid (lawnmower) flight lines to obtain uniform coverage across the plot network.

Table 1. Per-plot summary for the manually paired subset used in per-tree evaluation. #Trees denotes the number of stems in each plot with a verified field-to-reconstruction association; the All row reports pooled statistics across all plots.

Plot	#Trees	DBH mean \pm sd (cm)	DBH range (cm)
1	22	31.67 \pm 5.11	25.6–43.3
2	27	28.23 \pm 5.18	15.0–34.8
3	25	26.26 \pm 7.08	7.9–44.3
4	16	24.52 \pm 7.30	9.8–34.0
5	22	28.18 \pm 4.13	17.8–34.3
6	23	27.02 \pm 6.49	11.3–36.7
7	19	20.87 \pm 7.60	10.2–38.4
8	17	29.25 \pm 6.38	13.4–39.0
9	19	27.32 \pm 8.61	11.8–55.7
10	20	29.53 \pm 4.20	21.1–36.9
All	210	27.39 \pm 6.73	7.9–55.7

corrections. For each plot, a survey-grade GNSS rover mounted on a survey pole and stabilized with a bipod was centered over the plot and occupied for 30 minutes in static mode while receiving RTCM corrections via an NTRIP caster. Plot-center coordinates were derived using a differential GNSS workflow, following forest-canopy positioning best-practice recommendations described by Strunk et al. [43]. Corrected plot-center coordinates were then exported for co-registration with the aerial products.

UAV RGB imagery. For the full set of plots, we collected overlapping RGB imagery using a DJI Matrice 4E in two campaigns. Imagery was captured with high overlap and mixed viewing geometry (including oblique views at 70 and 90 m altitude) to support SfM/MVS reconstruction and increase the chance of observing trunk surfaces through gaps in the canopy and understory. To improve absolute positioning consistency across flights, we corrected the onboard UAV GNSS trajectory via post-processed kinematic (PPK) processing using reference data from a nearby CORS station (ARMO), and used the corrected solution to update image geotags before reconstruction. An example UAV RGB flight trajectory is shown in Figure 4(a).

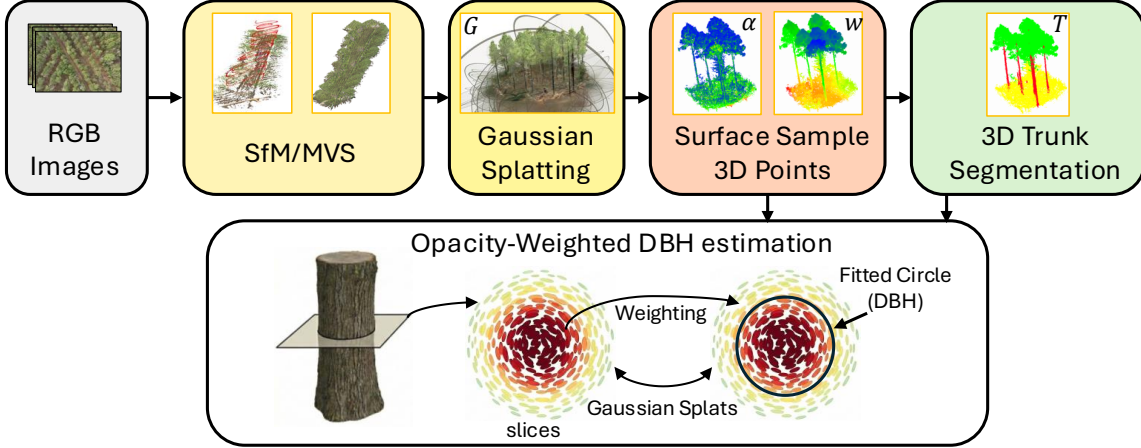


Figure 5. **TreeDGS pipeline.** RGB images are reconstructed with SfM/MVS and represented as 3D Gaussian splats G . We surface-sample dense points using opacity α and weights w , segment trunks T , and estimate DBH by opacity-weighted circle fitting on trunk slices.

UAV LiDAR We acquired UAV laser scanning (ULS) data with an Inertial Labs RESEPI payload integrating a Hesai XT-32 LiDAR. The XT-32 is a 360° mid-range scanner with a 0.05–120 m ranging capability and up to 640k pts/s in single-return mode, with typical range precision of 0.5 cm (1σ) and ranging accuracy of ± 1 cm [11, 16]. Figure 4(b) summarizes the LiDAR flight paths. The LiDAR survey used dense, back-and-forth flight lines (a lawnmower grid) to provide uniform coverage and reduce directional bias in canopy and stem observations. Flights were flown at ≈ 50 m above ground level, yielding point density of $\approx 1,407$ pts/m². The resulting georeferenced point clouds serve as a baseline geometry source for trunk isolation and DBH fitting.

Manual field-to-reconstruction association. Across all plots, we measured 458 stems in the field. We manually paired 210 pine stems (the target species in this study) with reconstructed trunk instances; Table 1 reports per-plot pine stem counts and DBH distribution statistics.

3. Proposed Pipeline

3.1. Problem Statement

Given a set of N high-resolution UAV RGB images $\{I_i\}_{i=1}^N$, our goal is to estimate the diameter at breast height (DBH) for each tree instance in the scene. DBH is defined as the trunk diameter at a fixed height above local ground, and we follow the field protocol used in this study ($h_{\text{BH}} \in [1.37, 1.40]$ m).

Our approach is geometry-driven: we reconstruct camera poses and an initial 3D structure with SfM, densify it with OpenMVS [4], optimize a Gaussian Splatting [22, 50] scene representation, and then measure DBH from trunk-

only geometry using opacity-aware sampling and robust fitting. Fig. 5 overviews the workflow; we summarize it as:

$$\{I_i\} \rightarrow (\{\mathbf{P}_i\}, \mathcal{X}_{\text{dense}}) \rightarrow \mathcal{G} \rightarrow \{\mathcal{T}_t\} \rightarrow \{\widehat{\text{DBH}}_t\}, \quad (1)$$

where \mathbf{P}_i are the calibrated camera matrices, $\mathcal{X}_{\text{dense}}$ is a densified point set from OpenMVS, \mathcal{G} is the optimized Gaussian field, and \mathcal{T}_t denotes trunk points for tree instance t .

3.2. Structure-from-Motion and Multi-View Stereo

We estimate camera poses and an initial scene structure using a Structure-from-Motion (SfM) pipeline [37] adapted to high-resolution UAV forest imagery, where repeated textures and partial occlusions can reduce matching reliability. To improve correspondence quality, we use a customized TopicFM [10] model trained on a mixture of (i) MegaDepth [28], (ii) 100 synthetic UAV nadir forest scenes, and (iii) 200 available real 3D models from the Coolant Dataset.

Coarse-to-fine matching. Because our UAV imagery is high resolution, we perform matching in a coarse-to-fine manner [26]: we first obtain coarse correspondences on downsampled images to establish robust global alignment, then refine matches locally at higher resolution. This reduces compute while maintaining accurate pixel localization needed for stable pose estimation.

SfM reconstruction. SfM takes the matched correspondences across overlapping image pairs and estimates: (i) camera poses $\{\mathbf{P}_i\}$ and (ii) a sparse 3D point set. We use standard robust estimation and bundle adjustment from GLOMAP [37] to refine the reconstruction. We denote the resulting calibrated cameras as:

$$\mathbf{P}_i = \mathbf{K}_i [\mathbf{R}_i \mid \mathbf{t}_i]. \quad (2)$$

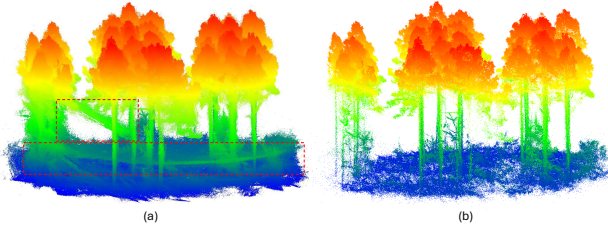


Figure 6. Comparison of back-projection points with multi-view depth consistency and the proposed sample points.

(a) Depth-fusion baseline: rendered depth points are back-projected into 3D and kept only if they pass multi-view depth-consistency checks. This produces large sheet-like artifacts near the ground/understory and incomplete stem surfaces (red dashed boxes), despite appearing consistent across views. (b) Our opacity-guided surface sampling with depth-aware point-wise compositing gives a stem geometry suitable for DBH estimation.

These cameras are used both for Gaussian training (Sec. 3.3) and for the multi-view opacity tests during surface sampling (Sec. 3.4).

Coarse densification with OpenMVS [4]. After SfM, we densify geometry using **OpenMVS**. OpenMVS produces depth information and a denser point set $\mathcal{X}_{\text{dense}}$, which provides stronger geometric support than the sparse SfM points in trunk regions. In our pipeline, $\mathcal{X}_{\text{dense}}$ serves as an initialization / prior for Gaussian optimization in Section 3.3.

3.3. Reconstruction with Gaussian Splats

Given calibrated cameras $\{\mathbf{P}_i\}$ and an MVS-densified initialization $\mathcal{X}_{\text{dense}}$ (Sec. 3.2), we optimize a 3D Gaussian Splatting (3DGS) scene representation. We adopt RaDe-GS [50], which builds on the real-time 3DGS renderer [22] while explicitly rasterizing depth in a way that is also useful for our subsequent surface-consistent point sampling.

Gaussian parameterization. The scene is represented as a set of anisotropic 3D Gaussians $G_k = (\boldsymbol{\mu}_k, \mathbf{s}_k, \mathbf{R}_k, \alpha_k, \mathbf{c}_k)$, where $\boldsymbol{\mu}_k \in \mathbb{R}^3$ is the Gaussian center, $\mathbf{s}_k \in \mathbb{R}_+^3$ are axis-aligned scales in the local frame, $\mathbf{R}_k \in SO(3)$ is the per-Gaussian orientation, $\alpha_k \in [0, 1]$ is the learned opacity, and \mathbf{c}_k denotes appearance parameters (e.g., spherical-harmonic features as in [22]). We initialize $\{\boldsymbol{\mu}_k\}$ from $\mathcal{X}_{\text{dense}}$ and optimize all parameters following RaDe-GS [50].

RaDe-GS depth-plane formulation. A key difference from vanilla 3DGS is that RaDe-GS associates each Gaussian and view with a local ray-distance plane in screen space. For a view v , let $\mathbf{u}_{k,v} \in \mathbb{R}^2$ be the projected mean of Gaussian k , and let $t_{k,v}$ be its ray-distance (range) in

that view (i.e., $\|\mathbf{R}_v \boldsymbol{\mu}_k + \mathbf{t}_v\|_2$ under perspective projection). RaDe-GS additionally provides a 2D slope $\mathbf{g}_{k,v} \in \mathbb{R}^2$, so that the Gaussian's predicted ray-distance at a nearby pixel \mathbf{u} is approximated by

$$d_{k,v}(\mathbf{u}) = t_{k,v} + \mathbf{g}_{k,v}^\top (\mathbf{u}_{k,v} - \mathbf{u}). \quad (3)$$

We use this depth-plane formulation in Section 3.4 to define a depth-aware, surface-consistent opacity integral at arbitrary 3D query points.

Adaptive training with RLGS. We integrate RLGS [29] as an online controller that adapts selected training hyperparameters based on observed optimization dynamics. In our setting, this is used to stabilize opacity and geometry quality for the downstream DBH pipeline. After convergence, the optimized Gaussian field is denoted \mathcal{G} and serves as the source representation for dense point sampling.

3.4. Surface Sampling with Opacity

Our downstream stages (3D trunk segmentation and DBH fitting) require a point cloud that is (i) dense enough to represent thin stems at stand-off distance and (ii) geometrically trustworthy under heavy occlusion from foliage and understory. This is not automatic from a 3D Gaussian Splatting (3DGS) reconstruction: the optimized field \mathcal{G} is a collection of overlapping volumetric primitives whose parameters are trained through front-to-back alpha compositing rather than an explicit surface loss [22, 50]. As a result, two seemingly straightforward exports are unreliable in our UAV forest regime. First, exporting one point per Gaussian (the means) produces a fragmented and extremely sparse cloud (Sec. 4, Fig. 10), which is insufficient for robust 3D segmentation and measurement. Second, back-projecting rendered depth maps into 3D and fusing them via multi-view depth-consistency preserves view-consistent sheet-like artifacts from semi-transparent vegetation while eroding already-scarce trunk evidence, especially when stems are only a few pixels wide or intermittently visible (Fig. 6). Therefore, we sample densely in 3D, but we accept and score samples using tests that are consistent with the same compositing model that governs 3DGS rendering and optimization.

Our goal is to convert the optimized Gaussian field \mathcal{G} into a point cloud that is dense enough for trunk segmentation and DBH fitting. For each Gaussian $G_i = (\boldsymbol{\mu}_i, \mathbf{s}_i, \mathbf{R}_i, \alpha_i)$, we draw candidate offsets $\boldsymbol{\xi}_{ij} \sim \mathcal{N}(\mathbf{0}, \mathbf{I}_3)$ in the local frame and map them to world coordinates. To focus sampling on reliable (high-opacity) regions, we apply Bernoulli thinning controlled by α_i :

$$\begin{aligned} \mathbf{p}_{ij} &= \boldsymbol{\mu}_i + \mathbf{R}_i (\mathbf{s}_i \odot \boldsymbol{\xi}_{ij}), \\ b_{ij} &\sim \text{Bernoulli}(\alpha_i). \end{aligned} \quad (4)$$

We keep \mathbf{p}_{ij} if $b_{ij} = 1$; in expectation each Gaussian contributes $\alpha_i M$ points when drawing M candidates.

In 3DGS, solidity is not defined by an explicit surface. It is defined implicitly by how Gaussians accumulate opacity under the renderer’s front-to-back alpha compositing. Therefore, any surface sampling rule that aims to match what the model learned should be expressed using the same compositing mechanism. For a view v and pixel \mathbf{u} , the renderer composites Gaussians front-to-back using transmittance tracking. If $\alpha_{k,v}(\mathbf{u})$ is the per-Gaussian alpha contribution at \mathbf{u} , we define $T_0(\mathbf{u}) = 1$ and update

$$\begin{aligned} w_{k,v}(\mathbf{u}) &= \alpha_{k,v}(\mathbf{u}) T_{k-1}(\mathbf{u}), \\ T_k(\mathbf{u}) &= T_{k-1}(\mathbf{u})(1 - \alpha_{k,v}(\mathbf{u})). \end{aligned} \quad (5)$$

so the accumulated alpha mask is $A_v(\mathbf{u}) = \sum_k w_{k,v}(\mathbf{u}) = 1 - T_{\text{final}}(\mathbf{u})$. In our code this mask is read from the renderer’s alpha channel and used as a visibility gate for sampled points.

The per-pixel accumulated alpha mask $A_v(\mathbf{u})$ tells us whether a ray intersects reconstructed mass somewhere along the ray, but it does not tell us whether a particular 3D sample \mathbf{p} lies on the visible surface, behind it, or in front of it (all can project to the same pixel). For surface extraction, we need a depth-aware test that measures how much opacity accumulates in front of \mathbf{p} along the viewing ray, using the same compositing model that governs training. RaDe-GS provides exactly this query by integrating point-wise alphas with a depth-plane formulation.

Beyond per-pixel alpha, RaDe-GS provides an integration query at an arbitrary 3D point \mathbf{p} : it returns the projected pixel coordinate $\mathbf{u}_v(\mathbf{p})$ and a cumulative opacity value $\tilde{\alpha}_v(\mathbf{p})$ that measures how much opacity is accumulated in front of \mathbf{p} along the viewing ray. Let $r_v(\mathbf{p}) = \|\mathbf{R}_v \mathbf{p} + \mathbf{t}_v\|_2$ denote the point ray-distance in view v . For a Gaussian k , RaDe-GS evaluates a ray-space quadratic form using a pre-computed inverse covariance over the 3D offset

$$\Delta \mathbf{u}_{k,v}(\mathbf{p}) = \begin{bmatrix} \mathbf{u}_{k,v} - \mathbf{u}_v(\mathbf{p}) \\ t_{k,v} - \min(r_v(\mathbf{p}), d_{k,v}(\mathbf{u}_v(\mathbf{p}))) \end{bmatrix}, \quad (6)$$

and converts it to an alpha contribution via an exponential falloff

$$\alpha_{k,v}(\mathbf{p}) \propto \alpha_k \exp\left(-\frac{1}{2} \Delta \mathbf{u}_{k,v}(\mathbf{p})^\top \Sigma_{k,v}^{-1} \Delta \mathbf{u}_{k,v}(\mathbf{p})\right). \quad (7)$$

The $\min(\cdot)$ depth clamping in Eq. (6) is critical for surface consistency: once \mathbf{p} lies behind the locally rasterized surface depth $d_{k,v}(\cdot)$, the depth residual term saturates rather than increases with $r_v(\mathbf{p})$, preventing spurious “volumetric” accumulation behind the surface. RaDe-GS composites these point-wise alphas using the same front-to-back transmittance as in Eq. (5), yielding the cumulative opacity

$$\tilde{\alpha}_v(\mathbf{p}) = \sum_k \alpha_{k,v}(\mathbf{p}) T_{k-1,v}(\mathbf{p}), \quad (8)$$

$$T_{k,v}(\mathbf{p}) = T_{k-1,v}(\mathbf{p})(1 - \alpha_{k,v}(\mathbf{p})).$$

Since DBH fitting is highly sensitive to even small amounts of geometric contamination, we aggregate evidence across the calibrated views and attach a per-point reliability that downstream steps can threshold or use as a weight. Concretely, we (i) only allow a view to contribute if the point projects to a foreground pixel in that view, and (ii) summarize the point-wise opacity integrals across contributing views conservatively. Let $\mathcal{P} = \{\mathbf{p}_{ij} \mid b_{ij} = 1\}$ be the candidate samples retained after the opacity-guided thinning in Eq. (4). For each $\mathbf{p} \in \mathcal{P}$, we evaluate its support over the calibrated views; a view v contributes only if \mathbf{p} projects inside the image and lands on a non-background pixel in the rendered accumulated alpha mask A_v . Specifically, with $\mathbf{u}_v(\mathbf{p})$ the projection of \mathbf{p} , we define

$$m_v(\mathbf{p}) = \mathbf{1}(A_v(\mathbf{u}_v(\mathbf{p})) > \tau_{\text{mask}}). \quad (9)$$

Then, we store two per-point reliability signals:

$$\bar{\alpha}(\mathbf{p}) = \min_{v: m_v(\mathbf{p})=1} \tilde{\alpha}_v(\mathbf{p}), \quad w(\mathbf{p}) = \sum_v m_v(\mathbf{p}). \quad (10)$$

Here $\bar{\alpha}(\mathbf{p})$ is a conservative multi-view opacity estimate, and $w(\mathbf{p})$ counts the number of views in which \mathbf{p} projects onto a foreground pixel, defined as a pixel whose rendered alpha exceeds τ . In practice, for surface extraction we keep points with $\bar{\alpha}(\mathbf{p}) > \tau$ and $w(\mathbf{p}) > 0$ (we use $\tau = 0.5$); for dense export we set $\tau = 0$ and keep all points while storing $(\bar{\alpha}, w)$ for downstream weighting.

3.5. Semantic Trunk Extraction

The sampled point cloud from Section 3.4 contains trunks mixed with foliage, understory vegetation, and occasional floating samples caused by Gaussians with nonzero opacity in free space. To isolate stem geometry for DBH measurement, we used ForestFormer3D [48], a 3D semantic segmentation model, to predict a class label for each sampled point and to assign per-tree instance IDs when available. In our pipeline, the per-point opacity reliability $\bar{\alpha}$ is kept as an auxiliary output feature alongside (x, y, z) . We retain only points predicted as trunk to form a trunk-only cloud for each tree instance t , denoted $\mathcal{T}_t = \{(\mathbf{x}_k, \bar{\alpha}_k)\}$. This separation step reduces contamination from branches and understory, while the retained opacity values enable reliability-weighted fitting downstream. Then, the trunk-only instances are passed to the DBH measurement stage.

3.6. Opacity-Weighted DBH Measurement

Given a trunk-only point set for tree instance t ,

$$\begin{aligned} \mathcal{T}_t &= \{(\mathbf{x}_k, \bar{\alpha}_k)\}_{k=1}^{N_t}, \\ \mathbf{x}_k &= (x_k, y_k, z_k)^\top \in \mathbb{R}^3, \quad \bar{\alpha}_k \in [0, 1]. \end{aligned} \quad (11)$$

our goal is to estimate the diameter at breast height (DBH), i.e., the trunk diameter at $h_{\text{BH}} \approx 1.3\text{--}1.4$ m

above local ground. A key challenge is that (i) the sampled points are volumetric (many points lie inside the trunk cross-section, not only on the boundary), and (ii) residual non-trunk points and floaters can persist even after segmentation. We address both issues using an opacity-weighted solid-circle RANSAC in each horizontal slice, followed by a robust height-wise taper regression.

DBH is defined relative to local ground height. For each tree instance, we estimate a ground elevation z_g by querying a digital terrain model (DTM) at the tree location (e.g., nearest-neighbor lookup at the mean trunk (x, y)), and convert all points to height-above-ground:

$$z_g = \text{DTM} \left(\frac{1}{N_t} \sum_{k=1}^{N_t} (x_k, y_k) \right), \quad h_k = z_k - z_g. \quad (12)$$

All subsequent slicing and DBH evaluation are performed in the (x, y) plane as a function of h .

We construct a sequence of slice centers $\{h_s\}$ with spacing Δz and thickness H (a slab of height H), and collect 2D points in each slab:

$$\begin{aligned} h_s &= s \Delta z, \quad s = 0, 1, \dots, \\ \mathcal{S}_s &= \left\{ (x_k, y_k, \bar{\alpha}_k) \mid |h_k - h_s| \leq \frac{H}{2} \right\}. \end{aligned} \quad (13)$$

Slices with fewer than a small minimum number of points (e.g., < 5) are discarded. This step produces a set of candidate diameters along the lower stem.

Unlike classical TLS stem fitting (where points often lie near the circumference), our sampling in Section 3.4 draws points from Gaussian volumes; therefore, many slice points legitimately fall inside the trunk cross-section. For this reason we treat inliers as belonging to a filled disk rather than a narrow ring around a circle. This choice makes the estimator consistent with volumetric sampling and substantially more stable under partial visibility.

Opacity-weighted solid-circle RANSAC in each slice. For slice s , we have 2D points $\{(\mathbf{q}_k, w_k)\}_{k=1}^n$ with $\mathbf{q}_k = (x_k, y_k)^\top$ and opacity weights $w_k = \bar{\alpha}_k$. Each RANSAC hypothesis performs the following steps:

(i) Weighted sampling: Draw three distinct indices (k_1, k_2, k_3) without replacement with $\Pr(k) \propto w_k$.

(ii) Circle fit from three points: Fit the circle through the sampled points using the algebraic form $x^2 + y^2 + ax + by + d = 0$. We solve for (a, b, d) after subtracting the slice mean (for numerical stability), then recover $\mathbf{c} = (-\frac{a}{2}, -\frac{b}{2})^\top$ and $r^2 = \|\mathbf{c}\|_2^2 - d$ (adding the mean back to \mathbf{c}).

(iii) Solid inliers and validity checks: A point is an inlier if it lies inside the disk: $\|\mathbf{q}_k - \mathbf{c}\|_2^2 \leq r^2$. We discard hypotheses whose radius r is abnormally large or that yield fewer than ρn inliers.

(iv) Opacity-weighted scoring: For the remaining hypotheses, we score

$$S(\mathbf{c}, r) = \frac{\sum_{k=1}^n w_k \mathbf{1}(\|\mathbf{q}_k - \mathbf{c}\|_2^2 \leq r^2)}{r^p}, \quad p > 0. \quad (14)$$

and select $(\hat{\mathbf{c}}_s, \hat{r}_s) = \arg \max_{\mathbf{c}, r} S(\mathbf{c}, r)$, reporting $\hat{d}_s = 2\hat{r}_s$.

Height-wise taper regression and DBH prediction. Even after per-slice robust fitting, some slices can be corrupted by branch attachments, residual foliage, or incomplete sampling. Therefore, we fit a simple taper model on the lower stem using RANSAC with a negative-slope prior:

$$\hat{d}(h) = \beta_0 + \beta_1 h, \quad \beta_1 < 0, \quad (15)$$

where RANSAC discards outlier slices and the slope constraint enforces physically plausible taper (diameter should not increase with height over short stem segments). In practice, we fit Eq. (15) over progressively larger height ranges starting near the ground (to avoid upper-canopy contamination) until a stable inlier set is found. Finally, DBH is reported as

$$\text{DBH} = \hat{d}(h_{\text{BH}}), \quad h_{\text{BH}} \in [1.37, 1.40] \text{ m}. \quad (16)$$

Role of opacity in robustness. The opacity weights $w_k = \bar{\alpha}_k$ originate from the multi-view rendering consistency test in Section 3.4. Points that are only weakly supported (e.g., floaters, thin vegetation, or ambiguous geometry) tend to have small $\bar{\alpha}$ and therefore (i) are sampled less often during hypothesis generation and (ii) contribute little to the inlier score in Eq. (14). This coupling between rendering-consistency and geometric fitting is the central mechanism behind our opacity-weighted measurement mode.

4. Experiments

4.1. Experimental settings

We evaluate TreeDGS on the 10 circular field plots described in Section 2. Field DBH was measured with a diameter tape at breast height ($h_{\text{BH}} = 1.37$ m above ground, Section 2). We compare direct DBH measurement under the following reconstruction sources and fitting strategies: (i) UAV LiDAR: DBH estimation from the aerial LiDAR point cloud using (a) cylinder fitting [32] and (b) our slice-wise circle fitting (non-weighted and intensity-weighted variants). (ii) TreeDGS: DBH estimation from the point cloud sampled from the optimized 3D Gaussian field (Section 3.4), using the same cylinder and circle fitting variants, with opacity-based weighting available only for TreeDGS. To ensure a fair comparison, trunk/instance segmentation for both LiDAR and TreeDGS inputs is performed using the same ForestFormer3D checkpoint [48].

Table 2. Per-plot DBH accuracy and robustness. RMSE/MAE/ME are in cm and RRMSE is in %. SR reports successful estimates over total trees. Bold indicates the best within each plot. TreeDGS with opacity-weighted circle fitting attains the best RMSE in 7/10 plots and the best aggregated performance.

Plot	Method	RMSE	RRMSE	MAE	ME	SR
		(cm)	(%)	(cm)	(cm)	(#/#)
All	LiDAR (Cyl. fit.)	7.91	28.85	5.04	1.64	187/190
	LiDAR (Cir. nw. fit.)	9.36	33.96	8.23	8.11	183/190
	LiDAR (Cir. w. fit.)	10.99	39.64	9.42	7.16	179/190
	TreeDGS (Cyl. fit.)	13.29	48.69	10.25	-6.46	189/190
	TreeDGS (Cir. nw. fit.)	9.61	35.22	6.97	5.79	189/190
	TreeDGS (Cir. w. fit.)	4.79	17.54	3.70	-0.38	189/190
1	LiDAR (Cyl. fit.)	6.09	19.53	4.68	-1.66	19/19
	LiDAR (Cir. nw. fit.)	6.58	21.10	5.62	4.60	19/19
	LiDAR (Cir. w. fit.)	6.25	20.13	5.50	5.01	18/19
	TreeDGS (Cyl. fit.)	11.69	37.47	10.99	-10.99	19/19
	TreeDGS (Cir. nw. fit.)	7.58	24.29	5.91	2.63	19/19
	TreeDGS (Cir. w. fit.)	4.94	15.83	3.72	-2.04	19/19
2	LiDAR (Cyl. fit.)	4.73	16.63	4.04	1.86	22/22
	LiDAR (Cir. nw. fit.)	8.87	31.20	7.68	7.68	22/22
	LiDAR (Cir. w. fit.)	8.47	29.80	7.28	4.01	22/22
	TreeDGS (Cyl. fit.)	13.43	47.21	9.84	-5.49	22/22
	TreeDGS (Cir. nw. fit.)	8.43	29.65	7.26	7.09	22/22
	TreeDGS (Cir. w. fit.)	5.07	17.82	3.18	1.88	22/22
3	LiDAR (Cyl. fit.)	17.22	66.04	9.85	7.77	20/20
	LiDAR (Cir. nw. fit.)	10.26	37.93	9.04	9.04	19/20
	LiDAR (Cir. w. fit.)	14.81	56.79	12.09	10.60	20/20
	TreeDGS (Cyl. fit.)	10.49	40.23	8.77	-7.35	20/20
	TreeDGS (Cir. nw. fit.)	16.39	62.83	9.47	8.15	20/20
	TreeDGS (Cir. w. fit.)	5.93	22.73	4.35	-0.10	20/20
4	LiDAR (Cyl. fit.)	6.24	25.47	5.15	4.12	16/16
	LiDAR (Cir. nw. fit.)	11.20	45.69	10.45	10.45	16/16
	LiDAR (Cir. w. fit.)	9.61	38.40	7.66	4.79	15/16
	TreeDGS (Cyl. fit.)	25.24	102.93	16.57	3.84	16/16
	TreeDGS (Cir. nw. fit.)	11.46	46.73	7.59	4.95	16/16
	TreeDGS (Cir. w. fit.)	5.74	23.40	4.53	-0.62	16/16
5	LiDAR (Cyl. fit.)	5.27	18.60	3.83	1.36	21/21
	LiDAR (Cir. nw. fit.)	8.42	29.69	7.92	7.92	20/21
	LiDAR (Cir. w. fit.)	13.62	47.99	12.86	12.86	20/21
	TreeDGS (Cyl. fit.)	12.39	43.69	11.01	-7.98	21/21
	TreeDGS (Cir. nw. fit.)	5.84	20.60	4.64	3.57	21/21
	TreeDGS (Cir. w. fit.)	4.38	15.46	4.01	-2.10	21/21
6	LiDAR (Cyl. fit.)	6.83	25.38	4.67	1.24	22/22
	LiDAR (Cir. nw. fit.)	8.91	33.09	7.75	7.59	22/22
	LiDAR (Cir. w. fit.)	10.99	40.83	9.69	8.56	22/22
	TreeDGS (Cyl. fit.)	8.64	32.10	7.91	-7.45	22/22
	TreeDGS (Cir. nw. fit.)	8.91	33.10	8.23	8.23	22/22
	TreeDGS (Cir. w. fit.)	3.15	11.72	2.48	0.91	22/22
7	LiDAR (Cyl. fit.)	5.06	23.52	4.18	0.04	15/17
	LiDAR (Cir. nw. fit.)	12.15	54.45	10.76	10.76	14/17
	LiDAR (Cir. w. fit.)	9.31	39.24	7.63	4.06	12/17
	TreeDGS (Cyl. fit.)	13.66	65.77	8.15	-0.28	17/17
	TreeDGS (Cir. nw. fit.)	12.01	57.81	10.57	9.68	17/17
	TreeDGS (Cir. w. fit.)	5.91	28.44	5.03	3.27	17/17
8	LiDAR (Cyl. fit.)	7.78	26.68	6.22	2.86	16/16
	LiDAR (Cir. nw. fit.)	10.06	34.52	8.42	8.42	16/16
	LiDAR (Cir. w. fit.)	12.19	40.37	11.37	7.55	15/16
	TreeDGS (Cyl. fit.)	11.83	40.59	10.97	-7.64	16/16
	TreeDGS (Cir. nw. fit.)	5.42	18.59	5.49	3.96	16/16
	TreeDGS (Cir. w. fit.)	3.68	12.63	3.14	-1.69	16/16
9	LiDAR (Cyl. fit.)	6.18	23.13	4.20	-0.38	16/16
	LiDAR (Cir. nw. fit.)	10.03	38.25	9.48	9.48	15/16
	LiDAR (Cir. w. fit.)	10.61	40.45	9.99	7.36	15/16
	TreeDGS (Cyl. fit.)	8.73	32.66	7.73	-7.73	16/16
	TreeDGS (Cir. nw. fit.)	8.50	31.81	6.85	5.17	16/16
	TreeDGS (Cir. w. fit.)	3.93	14.72	3.08	-1.26	16/16
10	LiDAR (Cyl. fit.)	4.34	14.71	3.67	-0.97	20/21
	LiDAR (Cir. nw. fit.)	7.51	25.42	6.76	6.76	20/21
	LiDAR (Cir. w. fit.)	10.58	35.82	9.42	5.03	20/21
	TreeDGS (Cyl. fit.)	12.07	40.88	11.40	-11.15	20/21
	TreeDGS (Cir. nw. fit.)	6.28	21.27	5.15	4.10	20/21
	TreeDGS (Cir. w. fit.)	4.42	14.95	3.73	-2.35	20/21

Cylinder fitting baseline. We follow DigiForests [32] for cylinder fitting. A cylinder is fit to each trunk point cloud using a RANSAC-initialized model. Each RANSAC round samples five points, estimates the cylinder center and axis

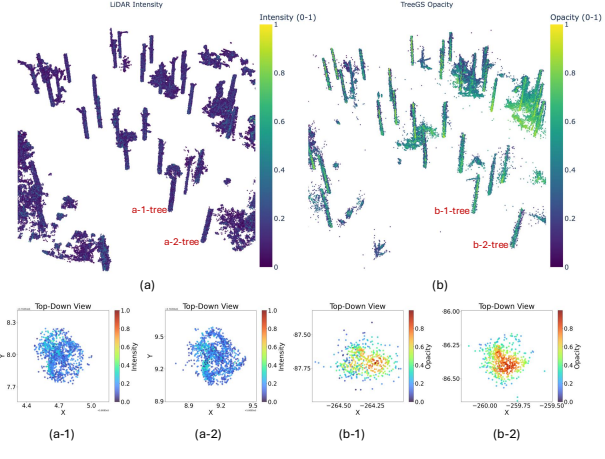


Figure 7. LiDAR intensity vs. TreeDGS opacity as a reliability signal at a same 5m slice height (Plot 2). (a) UAV LiDAR point cloud colored by normalized return intensity. (b) TreeDGS surface samples colored by learned opacity (0–1). Bottom: zoomed top-down views of two example stems ((a-1),(a-2) intensity; (b-1),(b-2) opacity). Compared to LiDAR intensity, the opacity values form a clearer high-confidence core around the stem cross-sections. This provides per-point confidence cue for DBH circle fitting. LiDAR has 281.4K points and TreeDGS has 66.6K points.

from the covariance SVD, and keeps models whose axis is within $\pi/8$ of vertical and radius ≤ 0.5 m. The RANSAC cylinder is then refined by least squares, updating the cylinder center, axis, and radius to minimize a robust (Geman–McClure) sum of squared point-to-cylinder distance residuals. Iterations stop when the parameter update norm falls below $\|\Delta x\| < 10^{-5}$, where $\Delta x \in \mathbb{R}^7$ stacks the center shift, rotation/axis update, and radius change. If the least-squares refinement increases the inlier ratio, it replaces the RANSAC estimate; otherwise the RANSAC cylinder is retained. Finally, the diameter at breast height is reported as DBH = $2r$ from the selected cylinder radius.

Circle fitting variants. For the proposed circle fitting, we evaluate two reliability modes: non-weighted (nw), which treats all points equally, and weighted (w), which uses a per-point reliability score as a weight (Eq. (10)) in both hypothesis sampling and inlier scoring (Eq. (14)). For TreeDGS, this reliability is the multi-view opacity consistency estimated by our renderer. For LiDAR, we additionally report an intensity-weighted analogue that uses normalized return intensity as a proxy weight. In our UAV data, this does not improve DBH accuracy because raw airborne LiDAR intensity is often speckled and unstable without careful radiometric correction and calibration (e.g., sensitivity to range, incidence angle, and scanner settings) [12, 19, 21, 46, 49]. Fig. 7 visualizes this gap: opacity

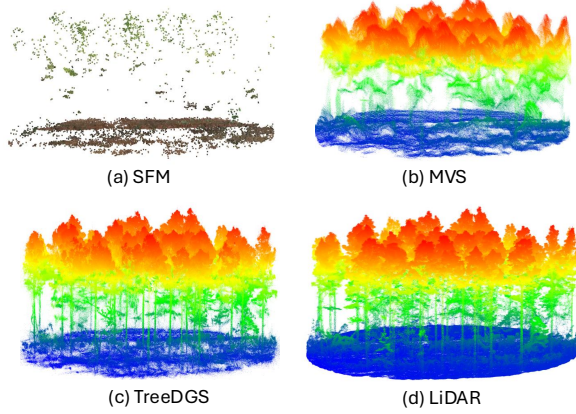


Figure 8. Qualitative comparison of point density and trunk completeness (Plot 1). (a) SfM points are sparse with limited stem coverage. (b) OpenMVS densification improves density but remains incomplete on trunks under canopy occlusion. (c) TreeDGS extracts a dense point set from the optimized Gaussians via opacity-guided sampling and RaDe-GS depth-aware cumulative-opacity tagging, yielding more continuous trunk support near breast height. (Max 100 candidate draws per splat; retained points vary with opacity.) (d) UAV LiDAR provides strong structure but can still be stem-sparse/contaminated depending on scan geometry and occlusion. Colors show height above ground.

yields a cleaner, geometry-aligned confidence core around stem cross-sections compared to noisy intensity. In addition, we omitted SfM/MVS benchmarking because breast-height trunk points were insufficient for stable segmentation and fitting in this dataset (See Fig. 8).

Across all circle-fitting variants, we use slice thickness $H = 1.0$ m and slice spacing $\Delta z = 0.1$ m, discarding slices with fewer than 5 points. For each slice, we run solid-circle RANSAC (Eq. (14)) with $K = 2000$ hypotheses, a minimum inlier fraction $\rho_{\min} = 0.1$, and radius bounds $r_{\min} = 0.02$ m and $r_{\max} = 1.0$ m. We set the radius regularization exponent to $p = 0.6$ via held-out validation on a 10% subset of the matched data and keep it fixed for all experiments, reporting results only on disjoint test data. The taper model in Eq. (15) uses RANSAC with residual threshold $\epsilon = 2$ cm (max trials $T = 1000$, min samples 3), requiring at least 10 inlier slices and enforcing $\beta_1 < 0$. Finally, DBH is reported as $\text{DBH} = \hat{d}(h_{\text{BH}})$ (Eq. (16)) evaluated at $h_{\text{BH}} = 1.37$ m.

We report four error measures between estimated and field DBH: root mean squared error (RMSE), relative RMSE (RRMSE, normalized by the mean field DBH), mean absolute error (MAE), and mean error (ME, bias). All errors are in cm, lower is better for RMSE/RRMSE/MAE, and ME closer to 0 indicates lower systematic bias.

4.2. Results

Table 2 summarizes per-plot performance and includes a pooled All row. TreeDGS with opacity-weighted circle fitting achieves the best overall accuracy (pooled RMSE = 4.79 cm; MAE = 3.70 cm) with negligible bias (ME = -0.38 cm), while maintaining a high success rate (189/190). Compared with the UAV LiDAR cylinder-fitting baseline, TreeDGS reduces pooled RMSE by approximately 39% while using only RGB imagery.

Ablations also show that the fitting model must match the reconstructed geometry. Applying a classical cylinder fit [32] to points sampled from TreeDGS performs poorly (13.29 cm RMSE; ME = -6.46 cm), consistent with our discussion in Section 3.6: TreeDGS sampling produces slice-wise cross-sections rather than a thin ring of surface points. Similarly, unweighted circle fitting is substantially less accurate (9.61 cm RMSE), showing that down-weighting low-confidence samples using multi-view opacity is a better approach.

TreeDGS (Cir. w. fit.) attains the lowest RMSE in most plots (Plots 1, 3–6, 8–9) and is within 0.34 cm RMSE of the LiDAR cylinder-fitting baseline in Plot 2 (Table 2). The largest gap appears in Plot 3: LiDAR (cyl. fit.) reaches 17.22 cm RMSE, whereas TreeDGS (Cir. w. fit.) remains at 5.93 cm, indicating greater robustness of alpha-opacity weighted in circle fitting.

Fig. 9 visualizes per-tree DBH errors. TreeDGS (cyl. fit.) exhibits a consistent underestimation trend (points below the 1:1 line), matching the negative pooled bias in Table 2. Unweighted circle fitting (TreeDGS (cir. nw. fit.)) shows greater scatter and occasional large overestimation, consistent with low-confidence samples inflating the fitted disk. In contrast, the opacity-weighted fit (TreeDGS (cir. w. fit.)) is more tightly clustered around the 1:1 line, indicating that multi-view rendering consistency provides a useful reliability cue for suppressing floating samples and occlusion-induced artifacts.

We additionally report a simple baseline that exports one point per Gaussian by using the splat centers $\{\mu_i\}$, similar to trunk-focused usage in prior 3DGS tree pipelines [27]. In our stand-off UAV forest scenes this produces an extremely sparse and surface-incomplete point set (Fig. 10), which breaks downstream instance segmentation with ForestFormer3D [48] and prevents reliable DBH fitting. These failures highlight that surface-densified sampling is necessary in the stand-off UAV setting.

5. Conclusion

We introduced TreeDGS: a UAV RGB-only pipeline that repurposes 3D Gaussian Splatting as an opacity-weighted density sampling method for trunk measurement, rather than only a view-synthesis renderer. Building on SfM/MVS

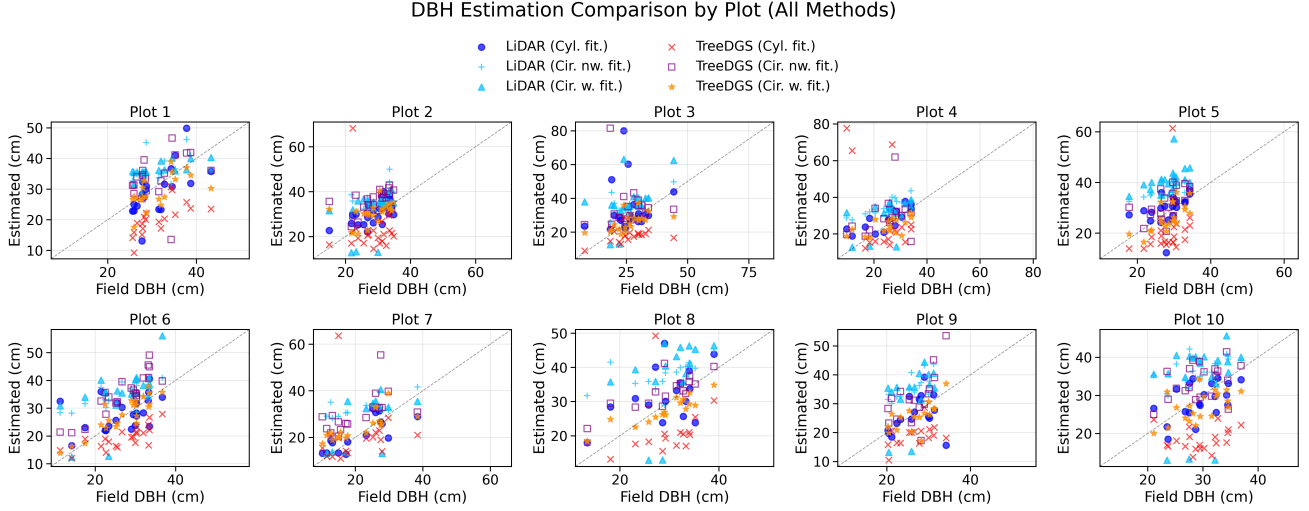


Figure 9. **Estimated vs. field DBH by plot (all methods).** Each panel shows per-tree predictions versus field tape measurements for one plot; the dashed line is the 1:1 reference. Across most plots, TreeDGS with opacity-weighted circle fitting clusters closer to the 1:1 line than unweighted fits and the TreeDGS+cylinder baseline, indicating reduced variance and substantially lower bias.

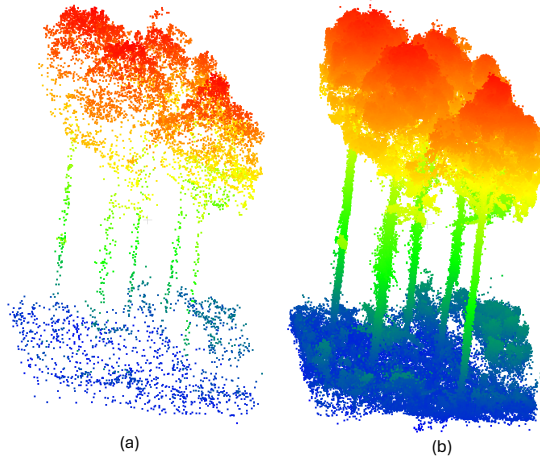


Figure 10. **Mean-only vs. proposed point sampling from Gaussian Splats.** (a) Exporting only Gaussian means [27] (one point per splat) yields an extremely sparse, fragmented cloud that is insufficient for downstream tasks such as 3D segmentation (ForestFormer3D [48]). (b) Our opacity-guided surface sampling densifies geometry and preserves stem surfaces and canopy structure.

initialization, TreeDGS optimizes a Gaussian field and then converts it into a measurement-ready stem point set via depth-aware cumulative-opacity sampling and multi-view reliability weighting, enabling robust circle fitting at breast height. This approach bridges a key gap left by prior UAV LiDAR and UAV-SfM DBH pipelines that operate on inherently sparse or view-limited point clouds [34, 35], and demonstrates that Gaussian splats can support accurate trunk-level metrics from commodity aerial imagery [22].

TreeDGS has important limitations. First, it relies on trunk visibility: the breast-height band must be observed in $\sim 2\text{--}3$ informative views for SfM/MVS and Gaussian optimization to constrain the stem surface. When this band is fully occluded in most views, the method cannot recover the missing geometry, regardless of how densely the Gaussian field is sampled; sampling density cannot compensate for geometry that is never sufficiently observed in the input imagery. Second, DBH estimation is sensitive to 3D semantic segmentation quality. Because diameter is fit from trunk-isolated points, false-positive trunk labels from nearby vegetation can bias the estimate. Although multi-view opacity weighting mitigates this effect, the pipeline remains subject to the failure modes of the trunk classifier [48]. This sensitivity can also contribute to poorer LiDAR baseline performance in challenging plots: breast-height stem returns with a small number of vegetation false positives can disproportionately bias cylinder fits.

A promising direction is to reduce dependence on post-processing (sampling and segmentation) by incorporating explicit trunk primitives into Gaussian optimization. Jointly optimizing a small set of parameterized stem elements (e.g., tapered cylinders) together with the Gaussian field would enable DBH to be inferred directly from model parameters and would provide a stronger inductive bias under partial trunk visibility. Such a hybrid representation may also support end-to-end supervision when ground-truth field DBH is available for future learning-based systems.

References

- [1] Karen Anderson and Kevin J. Gaston. Lightweight unmanned aerial vehicles will revolutionize spatial ecology. *Frontiers in Ecology and the Environment*, 11(3):138–146, 2013. 1
- [2] Sandra Brown. Estimating biomass and biomass change of tropical forests: A primer. Technical Report 134, Food and Agriculture Organization of the United Nations (FAO), Rome, Italy, 1997. 2
- [3] California Air Resources Board. Compliance offset protocol: U.s. forest projects. Technical report, California Environmental Protection Agency, 2015. Adopted June 25, 2015. 2
- [4] Dan Cernea. Openmvs: open multi-view stereo reconstruction library. <https://github.com/cdcseacave/openMVS>. Accessed: 2026-01-09. 4, 5
- [5] Jérôme Chave, Maxime Réjou-Méchain, Alberto Bürquez, and et al. Improved allometric models to estimate the aboveground biomass of tropical trees. *Global Change Biology*, 20(10):3177–3190, 2014. 2
- [6] Ziyue Chen, Bingbo Gao, and Bernard Devereux. State-of-the-art: Dtm generation using airborne lidar data. *Sensors*, 17(1):150, 2017. 2
- [7] Ismael Colomina and Pere Molina. Unmanned aerial systems for photogrammetry and remote sensing: A review. *ISPRS Journal of Photogrammetry and Remote Sensing*, 92:79–97, 2014. 1
- [8] Jonathan P. Dandois and Erle C. Ellis. High spatial resolution three-dimensional mapping of vegetation spectral dynamics using computer vision. *Remote Sensing of Environment*, 136:259–276, 2013. 2
- [9] Yasutaka Furukawa and Jean Ponce. Accurate, dense, and robust multi-view stereopsis. *IEEE Transactions on Pattern Analysis and Machine Intelligence*, 32(8):1362–1376, 2010. 2
- [10] Khang Truong Giang, Soohwan Song, and Sungho Jo. Topicfm+: Boosting accuracy and efficiency of topic-assisted feature matching. *IEEE Transactions on Image Processing*, 2024. 4
- [11] Hesai Technology. XT16/32/32M high-precision 360° mid-range lidar: Specification details (xt32). <https://www.hesaitech.com/product/xt16-32-32m/>. Accessed 2026-01-15. 4
- [12] Bernhard Höfle and Norbert Pfeifer. Correction of laser scanning intensity data: Data and model-driven approaches. *ISPRS Journal of Photogrammetry and Remote Sensing*, 62(6):415–433, 2007. 8
- [13] Markus Hollaus, Wolfgang Wagner, Bernhard Maier, and Klemens Schadauer. Airborne laser scanning of forest stem volume in a mountainous environment. *Sensors*, 7(8):1559–1577, 2007. 2
- [14] Hongyu Huang, Guoji Tian, and Chongcheng Chen. Evaluating the point cloud of individual trees generated from images based on neural radiance fields (nerf) method. *Remote Sensing*, 16(6):967, 2024. 2
- [15] Jakob Iglhaut, Carlos Cabo, Stefano Puliti, Livia Piermattei, James O'Connor, and Jacqueline Rosette. Structure from motion photogrammetry in forestry: a review. *Current Forestry Reports*, 5(3):155–168, 2019. 2
- [16] Inertial Labs. *RESEPI™ Hesai XT-32 Datasheet (rev. 1.03)*, 2024. Accessed 2026-01-15. 4
- [17] IPCC. 2006 ipcc guidelines for national greenhouse gas inventories, volume 4: Agriculture, forestry and other land use. Technical report, Intergovernmental Panel on Climate Change (IPCC) / IGES, 2006. 2
- [18] Jennifer C. Jenkins, David C. Chojnacky, Linda S. Heath, and Richard A. Birdsey. National-scale biomass estimators for united states tree species. *Forest Science*, 49(1):12–35, 2003. 2
- [19] Sanna Kaasalainen, Ulla Pyysalo, Anssi Krooks, Ants Vain, Antero Kukko, Juha Hyyppä, and Mikko Kaasalainen. Absolute radiometric calibration of ALS intensity data: Effects on accuracy and target classification. *Sensors*, 11(11):10586–10602, 2011. 8
- [20] Ville Kankare and et al. Diameter distribution estimation with laser scanning based multi-scan single-tree inventory. *ISPRS Journal of Photogrammetry and Remote Sensing*, 2015. 2
- [21] Alireza G. Kashani, Michael J. Olsen, Christopher E. Parrish, and Nicholas Wilson. A review of LiDAR radiometric processing: From ad hoc intensity correction to rigorous radiometric calibration. *Sensors*, 15(11):28099–28128, 2015. 8
- [22] Bernhard Kerbl, Georgios Kopanas, Thomas Leimkühler, and George Drettakis. 3d gaussian splatting for real-time radiance field rendering. *ACM Trans. Graph.*, 42(4):139–1, 2023. 2, 4, 5, 10
- [23] Adam Korycki, Cory Yeaton, Gregory S Gilbert, Colleen Josephson, and Steve McGuire. Nerf-accelerated ecological monitoring in mixed-evergreen redwood forest. *Forests*, 16(1):173, 2025. 2
- [24] Mikko Kukkonen, Matti Maltamo, Lauri Korhonen, and Petteri Packalen. Evaluation of UAS LiDAR data for tree segmentation and diameter estimation in boreal forests using trunk- and crown-based methods. *Canadian Journal of Forest Research*, 52(5):674–684, 2022. 2
- [25] Karel Kuželka, Martin Slavík, and Peter Surový. Very high density point clouds from UAV laser scanning for automatic tree stem detection and direct diameter measurement. *Remote Sensing*, 12(8):1236, 2020. 2
- [26] Vincent Leroy, Yohann Cabon, and Jérôme Revaud. Grounding image matching in 3d with mast3r. In *Eu-*

ropean Conference on Computer Vision, pages 71–91. Springer, 2024. 4

[27] Jiaqi Li, Qingqing Huang, Xin Wang, Benye Xi, Jie Duan, Hang Yin, and Lingya Li. A method for the 3d reconstruction of landscape trees in the leafless stage. *Remote Sensing*, 17(8):1473, 2025. 2, 9, 10

[28] Zhengqi Li and Noah Snavely. Megadepth: Learning single-view depth prediction from internet photos. In *Proceedings of the IEEE conference on computer vision and pattern recognition*, pages 2041–2050, 2018. 4

[29] Zhan Li, Huangying Zhan, Changyang Li, Qingan Yan, and Yi Xu. Rlgs: Reinforcement learning-based adaptive hyperparameter tuning for gaussian splatting. *arXiv preprint arXiv:2508.04078*, 2025. 5

[30] Xinlian Liang, Juha Hyypä, and et al. Terrestrial laser scanning in forest inventories. *ISPRS Journal of Photogrammetry and Remote Sensing*, 115:63–77, 2016. 2

[31] Kevin Lim, Paul Treitz, Michael Wulder, Benoît St-Onge, and Martin Flood. Lidar remote sensing of forest structure. *Progress in Physical Geography*, 27(1): 88–106, 2003. 2

[32] Meher VR Malladi, Nived Chebrolu, Irene Scacchetti, Luca Lobefaro, Tiziano Guadagnino, Benoît Casseau, Haedam Oh, Leonard Freiβmuth, Markus Karppinen, Janine Schweier, et al. Digiforests: a longitudinal lidar dataset for forestry robotics. In *2025 IEEE International Conference on Robotics and Automation (ICRA)*, pages 1459–1466. IEEE, 2025. 1, 7, 8, 9

[33] Ben Mildenhall, Pratul P. Srinivasan, Matthew Tancik, Jonathan T. Barron, Ravi Ramamoorthi, and Ren Ng. NeRF: Representing scenes as neural radiance fields for view synthesis, 2020. 2

[34] Bruno Miguez Moreira, Gabriel Goyanes, Pedro Pina, Oleg Vassilev, and Sandra Heleno. Assessment of the influence of survey design and processing choices on the accuracy of tree diameter at breast height (DBH) measurements using UAV-based photogrammetry. *Drones*, 5(2):43, 2021. 2, 10

[35] Romain Neuville, Jordan Steven Bates, and François Jonard. Estimating forest structure from uav-mounted lidar point cloud using machine learning. *Remote Sensing*, 13(3):352, 2021. 2, 10

[36] Francesco Nex and Fabio Remondino. Uav for 3d mapping applications: A review. *Applied Geomatics*, 6(1):1–15, 2014. 1

[37] Linfei Pan, Daniel Barath, Marc Pollefeys, and Johannes Lutz Schönberger. Global Structure-from-Motion Revisited. In *European Conference on Computer Vision (ECCV)*, 2024. 4

[38] Pasi Raumonen, Mikko Kaasalainen, Markku Åkerblom, Sanna Kaasalainen, Harri Kaartinen, Mikko Västaranta, Markus Holopainen, and Philip Lewis. Fast automatic precision tree models from terrestrial laser scanning data. *Remote Sensing*, 5(2): 491–520, 2013. 2

[39] Christian Salas, Liviu Ene, Timothy G. Gregoire, Erik Næsset, and Terje Gobakken. Modelling tree diameter from airborne laser scanning derived variables: A comparison of spatial statistical models. *Remote Sensing of Environment*, 114(6):1277–1285, 2010. 2

[40] Johannes L. Schönberger and Jan-Michael Frahm. Structure-from-Motion Revisited. In *Proceedings of the IEEE Conference on Computer Vision and Pattern Recognition (CVPR)*, 2016. 2

[41] Joe H. Scott and Elizabeth D. Reinhardt. Assessing crown fire potential by linking models of surface and crown fire behavior. Research Paper RMRS-RP-29, U.S. Department of Agriculture, Forest Service, Rocky Mountain Research Station, 2001. 2

[42] Belal Shaheen, Matthew David Zane, Bach-Thuan Bui, Shubham, Tianyuan Huang, Manuel Merello, Ben Scheelk, Steve Crooks, and Michael Wu. Forest-splat: Proof-of-concept for a scalable and high-fidelity forestry mapping tool using 3d gaussian splatting. *Remote Sensing*, 17(6):993, 2025. 2

[43] Jacob L. Strunk, Stephen E. Reutebuch, Robert J. McGaughey, and Hans-Erik Andersen. An examination of gnss positioning under dense conifer forest canopy in the pacific northwest, usa. *Remote Sensing Applications: Society and Environment*, 37(3):101428, 2025. 3

[44] Luke Wallace, Arko Lucieer, and et al. Assessment of forest structure using two UAV techniques: A comparison of airborne laser scanning and structure from motion. *Forests*, 7(3):62, 2016. 2

[45] Joanne C. White, Michael A. Wulder, Mikko Västaranta, Nicholas C. Coops, Douglas Pitt, and Murray Woods. The utility of image-based point clouds for forest inventory: A comparison with airborne laser scanning. *Forests*, 4(3):518–536, 2013. 2

[46] Qiong Wu, Ruofei Zhong, Pinliang Dong, You Mo, and Yunxiang Jin. Airborne LiDAR intensity correction based on a new method for incidence angle correction for improving land-cover classification. *Remote Sensing*, 13(3):511, 2021. 8

[47] Michael A. Wulder, Christopher W. Bater, Nicholas C. Coops, Thomas Hilker, and Joanne C. White. The role of lidar in sustainable forest management. *The Forestry Chronicle*, 84(6):807–826, 2008. 2

[48] Binbin Xiang, Maciej Wielgosz, Stefano Puliti, Kamil Král, Martin Krůček, Azim Missarov, and Rasmus Astrup. Forestformer3d: A unified framework for end-to-end segmentation of forest lidar 3d point clouds. In

Proceedings of the IEEE/CVF International Conference on Computer Vision (ICCV), 2025. [6](#), [7](#), [9](#), [10](#)

- [49] Wai Yeung Yan and Ahmed Shaker. Airborne LiDAR intensity banding: Cause and solution. *ISPRS Journal of Photogrammetry and Remote Sensing*, 142: 301–310, 2018. [8](#)
- [50] Baowen Zhang, Chuan Fang, Rakesh Shrestha, Yixun Liang, Xiaoxiao Long, and Ping Tan. Rade-gs: Rasterizing depth in gaussian splatting. *arXiv preprint arXiv:2406.01467*, 2024. [1](#), [2](#), [4](#), [5](#)